ADVANCED MATERIALS
www.advmat.de

Morphing Metal–Polymer Janus Particles

*Lewis M. Cox, Jason P. Killgore, Zhengwei Li, Zheng Zhang, Donna C. Hurley, Jianliang Xiao, and Yifu Ding**

Shape-memory polymers have the unique ability to memorize and recover their permanent shapes after being programmed to hold high strain levels up to a few hundred percent. Although studies have traditionally focused on utilizing shape-memory effects for macroscale applications, such as surgical stents and sutures,[1] as well as temperature sensors,[2] recent work has highlighted the potential of polymers to memorize and recover sub-micrometer surface patterns.[3–5] However, polymeric micro- and nanoparticles, ranging from structurally homogeneous to core-shell to Janus particles, already enjoy wide interest owing to their uses in drug delivery, electronic packaging, optical biosensors, and test beds for the mechanosensitivity of cells.[6–9] Incorporating shape-memory effects—that is, the ability to change shape on external stimuli—into these current polymer-particle-based technological platforms could potentially lead to a host of new engineering applications. However, the ability of micro- and nanoparticles to successfully fix large three-dimensional (3D) strains and recover their permanent shapes has not yet been investigated. Here we demonstrate the successful programming of large compressive engineering strains in crosslinked polymer microparticles via nanoimprint lithography (NIL). The recovery of these particles is shown to depend strongly on the constraints of substrates and superstrates, the latter of which is shown to generate a series of rosette-like smart Janus particles.

NIL is a reliable, high-throughput fabrication technique that is capable of compressing two parallel rigid substrates by use of high pressures.[10,11] The programming and recovery of polystyrene (PS) particles with NIL are illustrated in **Figure 1**a. The model PS spheres used were lightly crosslinked with 2% divinylbenzene (4.25 μm diameter) and were first deposited on a silicon (Si) wafer with a native silicon oxide (SiO_x) surface layer via dip-coating. The particles were then "imprinted" with a flat mold (Si wafer) at 120 °C (glass transition temperature, T_g, of PS ≈100 °C) under a relatively high pressure (1.5 MPa). The deformed PS particles were cooled to room temperature, which is well below their T_g, to fix the temporary disc-like shape after pressure release. Scanning electron microscopy (SEM) images show that following this procedure, deposited particles (Figure 1b) are successfully programmed to hold highly strained temporary shapes (Figure 1c), with compressive ratios (defined as the ratio of the difference between the original height and the compressed height to the original height of the particle) as large as 0.931.

When these deformed particles are annealed at 120 °C for a period of 1 h, they exhibit significant recoveries of their permanent shapes (Figure 1d). Depending on the initial compression ratio, the height of the recovered particles ranged from 72% to 90% of its original value (Figure 1e). On the basis of the low (<10°) contact angle between similar PS microspheres and SiO_x surfaces,[12] the shape recovery (Figure 1c–d) is driven by elastic strain energy release rather than surface energy minimization between the particles and the substrate. The side-view profiles of these particles (Figure 1d, inset) revealed that a relatively large contact radius of (2.1 ± 0.8) μm (standard deviation, $N = 7$) still exists between the PS and SiO_x interface after annealing, resulting in the incomplete recovery of the PS particles (Figure 1e). This residual contact radius is much larger than the equilibrium contact radius (≈0.66 μm) between the rubbery PS particle and the Si wafer, as estimated from the traditional JKR model (see calculation in Supporting Information).[13] The residual contact radii are results of either viscous or plastic deformation during the compressions and/or the work of adhesion between the PS and Si substrate. Both factors could increase with the larger compression ratios, leading to the lower degrees of recovery shown in Figure 1e. This adhesive contact effect can be alleviated by sonicating to release the compressed PS particles off the Si wafer and then re-depositing them onto a freshly prepared Si wafer. After annealing at 120 °C for 1 h, re-deposited PS particles recovered (96.1 ± 0.8)% ($N = 9$) of the initial height, as these particles do not form as intimate a contact with the wafers as those in Figure 1e.

Previous studies have reported both strain-hardening effects during the compression of micro-particles and the presence of non-homogeneous cross-linking densities that structurally form a stiffer shell with a softer particle core.[14] To assess whether or not these characteristics affect the PS particle deformations during compression, the geometries of programmed PS particles (Figure 1c) were analyzed. In particular, Figure 1f plots the lateral deformation ratio (the ratio of the overall lateral extension of the compressed particle to the diameter of the uncompressed particle) as a function of compression ratio. Compared with the theoretical and experimental deformation geometries of centimeter-scale rubber balls, which are accurately modeled as incompressible solids,[15] the compressed PS micro-particles exhibit no obvious deviation. In order to capture the particle geometries during recovery, we annealed the compressed particles at 110 °C. At this temperature, shape

L. M. Cox, Z. Li, Z. Zhang, Prof. J. Xiao, Prof. Y. Ding
Department of Mechanical Engineering
University of Colorado at Boulder
Boulder, CO 80309–0427, USA
E-mail: yifu.ding@colorado.edu
J. P. Killgore, D. C. Hurley
Applied Chemicals and Materials Division
National Institute of Standards and Technology
Boulder, CO 80305, USA

DOI: 10.1002/adma.201304079

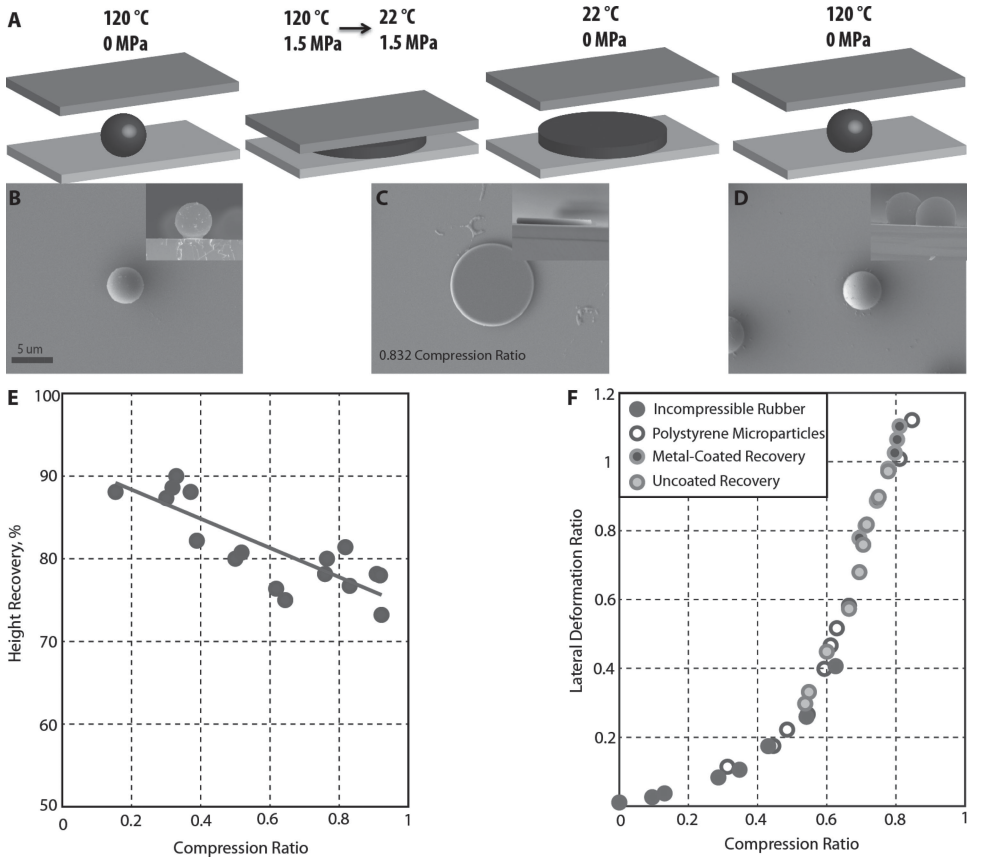

Figure 1. A) Illustration of the programming of polymer particles with NIL and their recovery. B,C,D) SEM images showing the PS particles after deposition, compression, and recovery. The insets are the corresponding cross-sectional view of the particles. The scale bar applies to all the images. E) The percentage of recovered particle height at 120 °C (with respect to the original height) decreases (trendline) as a function of the compression ratio (ratio between the height of the compressed particle and that of the uncompressed one). F) The lateral dimensions of the compressed PS micro-particles as a function of compression ratio compared to the dimensions of centimeter-scale rubber balls,[15] as well as recovering PS particles and recovering particles with a 10.2 nm Au-capping layer (the latter two recovered at 110 °C).

recovery rate is slower compared to that at 120 °C,[16] which allows in situ heated-stage atomic force microscope (AFM) imaging of the particle shapes. From the measurements, the lateral deformation and compression ratios of the recovering particles exhibit relationships similar to those in compressed particles (Figure 1f). This relationship is crucial for the morphological development of metal-film-capped recovery described below.

In addition to the SiO_x substrate, a thin metal layer deposited on top of the programmed PS particles can also constrain their shape recovery. For bulk shape-memory polymers, such metal-film-constrained recoveries give rise to a range of wrinkling patterns, which has recently attracted much attention.[17–20] In the following, we show that metal-layer constrained recovery in the above programmed PS particles creates a series of intricate and controllable wrinkle patterns, which have never before been observed. Au films with varying thicknesses were deposited on top of the compressed PS particles by use of a thermal evaporator. The Au film thickness (which varied less than 2% across the sample) was subsequently determined via AFM by scanning across the edges of the ring left after the compressed particles had recovered, thus exposing bare silicon substrate (as marked by the dotted line in **Figure 2**a). The sizes of the rings also mark lateral expansion of the compressed PS before metal deposition. During the metal deposition, no particle recovery due to heating from thermal evaporation was observed.

Figure 2 shows the evolution of wrinkle patterns during the recovery of a compressed PS particle capped with a 10.2 nm Au film. In order to slow down recovery and capture the early-stage morphologies, we once again annealed the Au-coated particles at 110 °C. After 45 s of annealing particles with compressive ratios of ≈0.88, a hierarchical wrinkle pattern emerged, consisting of azimuthally oriented wrinkles along the particle edges (Figure 2a, top inset) and labyrinthine wrinkles in the central regions (Figure 2a, bottom inset). Note that in this study, wrinkling refers to any observable change in surface morphology and does not distinguish between elastic deformation and plastic buckling of the thin metal films. With annealing time increased to 5 min (Figure 2b) or 60 min (Figure 2c), no significant changes were observed in the overall features of the hierarchical wrinkles. Specifically, the period or correlation length of the azimuthal wrinkles grows only slightly with the increase of annealing time (Figure 2e). While Figures 2a–c are images of different particles (with similar compression ratios), in situ

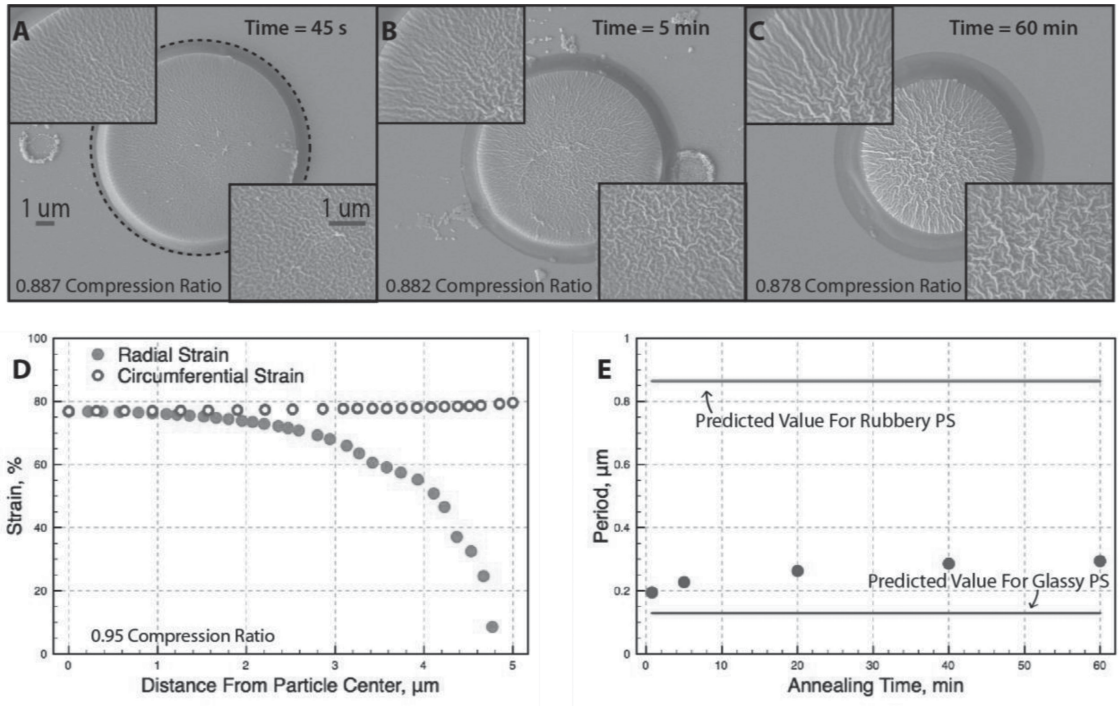

Figure 2. A–C) SEM images of wrinkling patterns on the surface of Au coated particles after being annealed at 110 °C for given durations as marked in each figure. The top and bottom insets are magnified views of the azimuthal wrinkles near the edge and labyrinthine wrinkles at the central region of annealed particles, respectively. The scale bars in (A) and in the inset of (A) apply to all primary images and insets, correspondingly. D) Circumferential and radial strains stored in the compressed particles. E) The azimuthal wrinkling periodicity as a function of annealing period at 110 °C. The two solid lines correspond to the upper and lower bound, assuming the rubbery modulus and glassy modulus of PS.

heated-stage AFM imaging of wrinkle formation of a single metal-capped particle during annealing is shown in Video S1 (Supporting Information). The video confirms that labyrinthine and azimuthal wrinkling domains remain fixed after their initial emergence, whereas the overall amplitude of the wrinkling morphology increases during the annealing process.

The hierarchical wrinkling patterns originate from the unique strain loading on the metal films during the particle recovery. From finite element analysis (FEA), the strain fields in the highly compressed particles consist of both strong circumferential and radial strains (Figure 2d). At the central region of the particles, the magnitude of these two perpendicular strains is comparable, effectively causing an equibiaxial-type (in cylindrical coordinates) compressive strain on the metal/polymer bilayer. This results in the labyrinthine type wrinkle patterns similar to those observed in planar bilayer system under biaxial compressive loading.[21] By contrast, near the edges of the compressed particles, the circumferential strains dominate, primarily creating uniaxial compressive strain loading during recovery. Note that a) the particles presented here exhibit compression ratios larger than 0.6, a deformation regime where changes in lateral strain are significantly greater than associated changes in vertical strain (Figure 1f), and that b) the wrinkling periodicity is significantly smaller than the bilayer radius of curvature, indicating that film curvature plays no significant role in the formation of wrinkling patterns. Accordingly, we compare the azimuthal wrinkling patterns to the sinusoidal wrinkling patterns observed in uniaxially compressed flat bilayers.[22,23] Specifically, surface wrinkling occurs when the uniaxial compressive strain exceeds a critical strain in the bilayer system,[24] ε_c: $\varepsilon_c = \frac{1}{4}\left(3\overline{E_s}/\overline{E_f}\right)^{2/3}$, where $\overline{E}$ represents the plane strain modulus $E/(1-\nu)^2$ that depends on Poisson's ratio ν and Young's modulus E of the materials, and the subscripts f and s refer to the film and substrate, respectively. Furthermore, the characteristic periodicity of the wrinkles is $\lambda_c = 2\pi t\left(\overline{E_f}/3\overline{E_s}\right)^{1/3}$,[21] where t is the thickness of the film. During the recovery of the Au-capped PS particles, the PS modulus drops three orders of magnitude, from 3.2 GPa to 10 MPa[25] (while the ν increases from 0.33 to ≈0.49), as the annealing temperature rises above the T_g of PS. Using plane strain modulus values of 98 GPa for the Au film,[26] the characteristic periodicities for the classical 10.2 nm thick Au-PS bilayer are 0.129 μm and 0.864 μm, assuming glassy and rubbery moduli of PS, respectively, as marked in Figure 2e. For the Au-coated PS particle (with compression ratio ≈ 0.83), the measured periodicity slightly increased with annealing time but remained close to the lower bound (associated with a more glassy PS substrate).

As compressed PS micro-discs were heated, the modulus started to decrease, triggering the shape recovery. The estimated critical strain needed to cause buckling in the Au film on a glassy PS substrate is 6%, a strain level not achievable by the glassy polymer without fracturing.[27] However, as the PS modulus drops during annealing, this critical strain decreases (to as low as 0.14% for a rubbery PS substrate), and wrinkling occurs

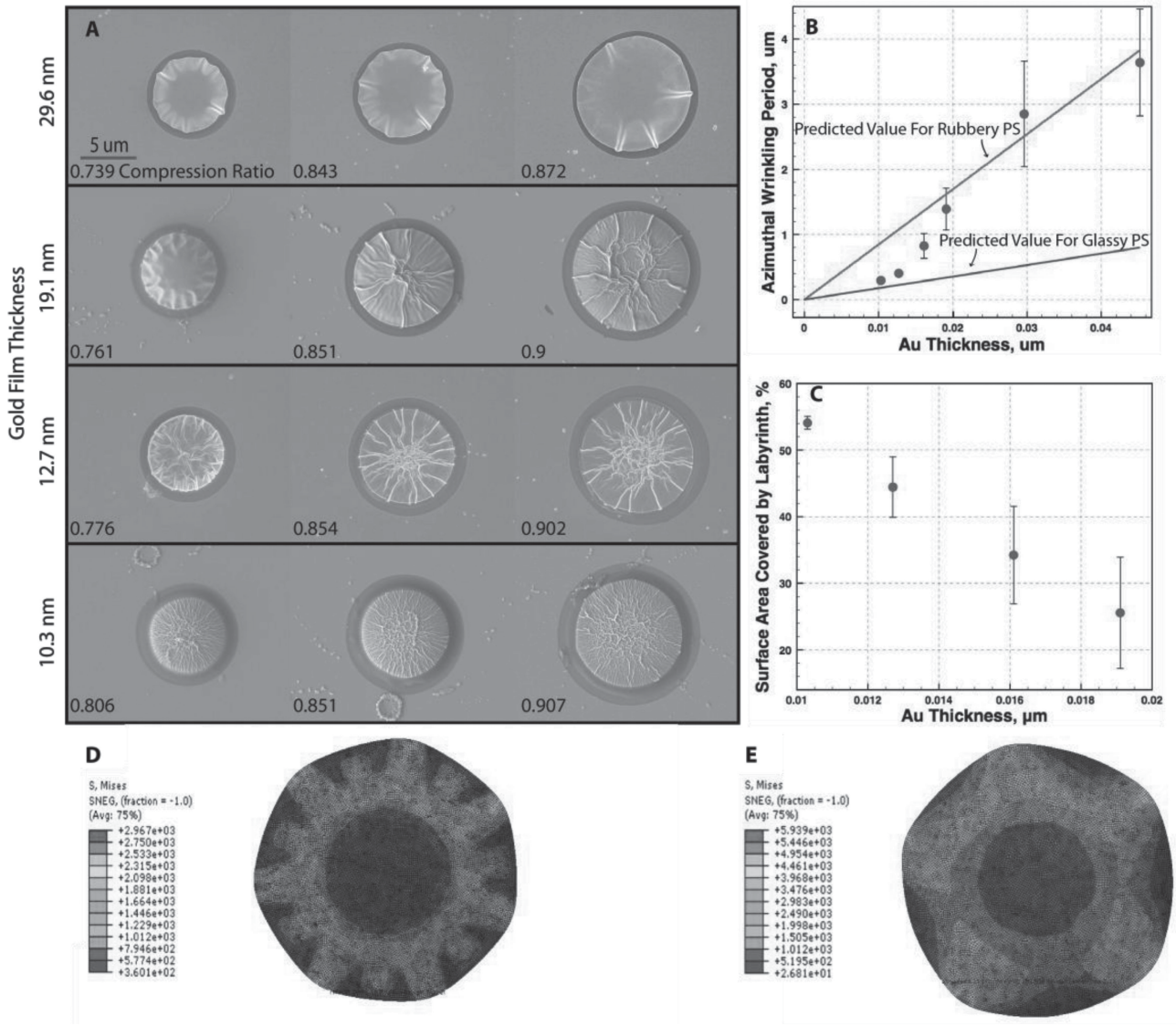

Figure 3. A) Wrinkling morphologies on the surface of Au coated particles after 1 hour of annealing at 110 °C, with varying Au film thicknesses and degrees of pre-strain (increasing left to right). The scale bar applies to all 12 images. B) The periodicity of azimuthal wrinkles at the outermost edges of the particles as a function of Au film thickness, compared to the theoretical wrinkling periodicity for glassy and rubbery PS. C) The areal coverage of the labyrinthine wrinkling patterns on the annealed particles as a function of Au film thickness. D,E) FEA simulations showing the azimuthal wrinkling patterns in particles deformed to compression ratios of 0.4 with Au capping layers of 5 nm and 10 nm, respectively.

when the recovered strain exceeds the critical value. After the wrinkles form (Figure 2a), increasing strain due to the continuous recovery leads to the growth in amplitude of the wrinkles, observed in Figure 2b and Figure 2c, consistent with the wrinkling of classical bilayer systems.[21] Although it was expected that the wrinkling periodicity would manifest near the rubbery bound, as glassy polymers are unable to exceed the critical strain necessary to induce wrinkling, the observation that the azimuthal periodicity is closer to the lower bound (predicted for a glassy PS substrate) may be due to additional adhesion constraints from the substrate, influence of curvature during annealing, and/or the increase of the PS modulus during the cooling step.

Figure 3a summarizes the morphologies of the Au-coated PS particles obtained after annealing at 110 °C for one hour, varying the compression ratio of the programmed PS particles as well as the thicknesses of the Au film. Along the edges of all annealed particles, azimuthal wrinkles dominate the surface topography. Varying compression ratios within the range shown in Figure 3 had no significant effect on the wrinkling periodicity observed for a given thickness of Au film. This type of strain-independence is expected when particle curvature effects do not dominate wrinkling morphologies, and the system behaves similarly to the classical case of bilayer buckling. However, the periodicity of the azimuthal wrinkles increases with the Au film thickness, and the periodicity shifts from being close to the lower bound (glassy PS) to the upper bound (rubbery PS) (Figure 3b). For Au films of 19.8 nm and thinner, labyrinthine wrinkling pattern forms in the center of the PS particles and its

areal coverage decreases with the increase of Au film thickness (Figure 3c). For Au films thicker than 19.8 nm, this type of labyrinthine wrinkling was not observed.

Limited by our current NIL setup—that is, a pressure-controlled compression—low compression ratios (below 0.5) are difficult to achieve. To examine the morphology of metal-constrained recovery on particles with low compression ratios, FEA simulations were carried out (Figure 3d,e). For a compression ratio of 0.4, the azimuthal wrinkles along the edges of the particles were still observed, but no labyrinthine wrinkles were present in the central region. As expected, the azimuthal wrinkle periodicity increased with metal film thickness. By comparison, the absence of labyrinthine wrinkling is due to the larger changes in out-of-plane strain relative to the accompanying lateral strains during the recovery of particles with lower compression ratios (Figure 1f). In other words, recovery in the vertical dimension is larger than the lateral dimensions, and the compressive forces inducing wrinkling morphologies are primarily driven by an increase of curvature. Such morphology has been observed in stiff films experiencing large out of plane strains.[28,29] Note that the current FEA system is not able to model wrinkling at the larger experimental compression ratios (Figure 3a), and a more rigorous analysis is currently underway to quantitatively understand the mechanical instabilities in this confined and curved buckling system.

The morphologies shown in Figure 3 can further evolve, given longer annealing time or higher annealing temperatures. **Figure 4**a shows the Au-coated PS particles after being annealed at 120 °C for one hour, which leads to higher degree of recovery and thus higher compressive strain on the system. The PS particles coated with 11.6 nm thick Au layers recovered into a rosette-type shape, where the azimuthal wrinkles become rougher, and the labyrinthine wrinkles have evolved into a highly folded shape. Such unique morphology has never before been demonstrated. It is known that hierarchical wrinkling can occur in the presence of larger compressive stresses when the amplitudes of the smaller, first-generation wrinkles saturate and effectively form a new, stiffer skin.[30] Similarly, the earlier-formed labyrinthine wrinkles are still discernible and are superimposed on the surfaces of these new protrusions (Figure 4). As the compression ratio increases, the central protrusion is seen to grow from an elegant, circular ridge to a larger, bowl-like shape.

To examine the generality of the wrinkled morphology generated during the constrained shape recovery, we also coated programmed PS particles with an 11.9 nm thick chromium (Cr) film. As shown in Figure 4b, the rosette structures are again observed, with a similar dependence on the compression ratio. According to the bilayer buckling analysis mentioned above, because of its larger modulus, the azimuthal wrinkling periodicity of the stiffer Cr film should be 47.6% larger than that of the Au. This is indeed observed experimentally: the average azimuthal periodicity along the edges of the Cr coated systems [(0.36 ± 0.07) μm, $N = 6$] is 44.0% larger than those associated with the Au coated system [(0.25 ± 0.03) μm, $N = 6$]. Such results suggest a significant predictability and reproducibility of these complex wrinkling structures applicable to generalized material systems not investigated here.

In conclusion, we demonstrate that lightly cross-linked PS micro-particles exhibit the ability to undergo shape-recovery after fixing large degrees of compression. This recovery behavior is shown to be highly dependent on the substrate confinement. Furthermore, these programmed particles can be used as the foundation for creating unprecedented, highly hierarchical surface features in the presence of metal coatings, which can be tuned by the degree of particle compression, thickness and stiffness of the capping layer, and annealing conditions.

The incorporation of shape-changing capability into polymer-based micro- and nanoparticles opens a new avenue for creating deployable smart particles. Compared with current, chemically activated smart particle technologies such as

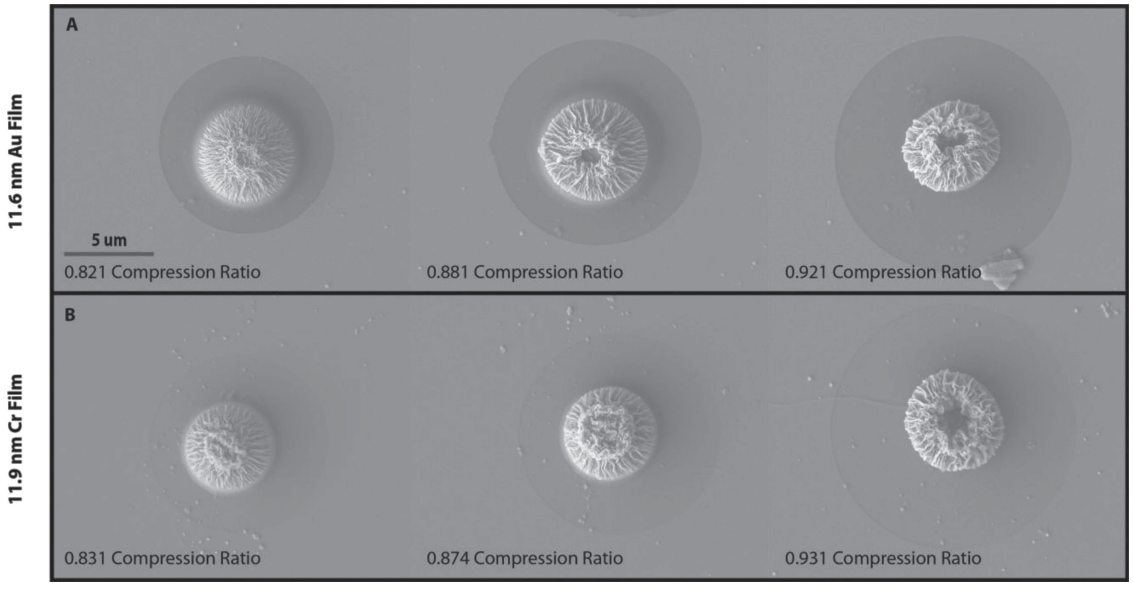

Figure 4. A) The wrinkling morphologies of particles with an 11.6 nm Au film after annealing for 1 h at 120 °C exhibit a rosette structure with a cup-like pocket in the center. B) Particles capped with an 11.9 nm Cr film and annealed result in similar rosette morphologies.

hydrogel particles[31] and liquid crystal particles,[32] the approach presented here is dramatically simplified and requires only a cross-linked particle capable of being physically strained to large degrees. Compared with static particles, such smart particles, which are capable of changing shape while either maintaining constant volume (via thermal triggering) or with simultaneous volume increase (via solvent triggering), can have exciting potential in applications of thermo-responsive composites and smart fluids with tunable rheological properties. Further, the constrained recovery with metal films offer a new approach to create smart, multifunctional Janus particles with unique combinations of contrasting properties, including both topography and physical and chemical properties, which are promising for applications in catalysis, drug delivery, and magnetic biomarkers.[33–35]

Experimental Section

Programming of Particles: PS particles with 4.25 µm diameter and 2% divinylbenzene cross-linker density (PS05N/5689, Bangs Laboratory Inc.) were deposited on a flat silicon wafer by dipping the wafer into an aqueous solution containing particles and then drawing it out at 1 mm s^{-1}. Prior to the NIL process, the silicon mold used for compression was first cleaned using piranha solution and coated with a low-surface-energy, self-assembled monolayer of $CF_3(CF_2)_5(CH_2)_2SiCl_3$ (tridecafluoro-1,1,2,2-tetrahydrooctyltrichlorosilane, Sigma-Aldrich) by vapor deposition to facilitate mold release from the particles after imprinting. All NIL processes were performed on a nanoimprinter (Eitre 3, Obducat) at 120 °C under a pressure of 1.5 MPa for 5 minutes. After this time period, the compressive force was maintained while the particles were cooled back to room temperature, at which point the pressure was relieved and the silicon mold was removed from the flattened particles. A thermal evaporator (SC-3000, CVC Products Inc.) was used to deposit metal films onto the surface of flattened particles.

Determination of Labyrinthine Areal Coverage: Images of wrinkled particles captured via SEM were divided into eighths by four axes drawn across the diameter of the particle surface (acute central angles of 45°). The domain along each given axis where wrinkles are observed to intersect at angles greater than 45° was measured, and the domain sizes across all 4 axes were averaged to obtain the effective diameter of labyrinthine area covering a given particle surface.

Supporting Information

Supporting Information is available from the Wiley Online Library or from the author.

Acknowledgements

We acknowledge the funding support from the National Science Foundation under grant number CMMI-1031785 and CMMI-1233626. Certain commercial equipment, instruments, or materials are identified in this paper in order to specify the experimental procedure adequately. Such identification does not imply recommendation or endorsement by NIST, nor does it imply that the materials or equipment identified are necessarily the best available for the purpose.

Received: August 18, 2013
Revised: August 28, 2013
Published online: October 25, 2013

[1] A. Lendlein, S. Kelch, *Angew. Chem. Int. Ed.* **2002**, *41*, 2034.
[2] C. Liu, H. Qin, P. T. Mather, *J. Mater. Chem.* **2007**, *17*, 1543.
[3] Z. Wang, C. Hansen, Q. Ge, S. H. Maruf, D. U. Ahn, H. J. Qi, Y. Ding, *Adv. Mater.* **2011**, *23*, 3669.
[4] H. Xu, C. Yu, S. Wang, V. Malyarchuk, T. Xie, J. A. Rogers, *Adv. Funct. Mater.* **2013**, *23*, 3299.
[5] K. A. Davis, K. A. Burke, P. T. Mather, J. H. Henderson, *Biomaterials* **2011**, *32*, 2285.
[6] M. Himmelhaus, H. Takei, *Sens. Actuators B* **2000**, *63*, 24.
[7] F. D. Benedetto, V. Fasano, L. Persano, C. Maruccio, E. Mele, G. Potente, D. A. Weitz, L. D. Lorenzis, D. Pisignano, *Soft Matter* **2013**, *9*, 2206.
[8] H. Vandeparre, S. Gabriele, F. Brau, C. Gay, K. K. Parker, P. Damman, *Soft Matter* **2010**, *6*, 5751.
[9] Q. Chen, E. Diesel, J. K. Whitmer, S. C. Bae, E. Luijten, S. Granick, *J. Am. Chem. Soc.* **2011**, *133*, 7725.
[10] S. Y. Chou, P. R. Krauss, P. J. Renstrom, *Science* **1996**, *272*, 85.
[11] L. J. Guo, *Adv. Mater.* **2007**, *19*, 495.
[12] R. Seemann, K. Jacobs, R. Blossey, *J. Phys. Condens. Matter* **2001**, *13*, 4915.
[13] K. L. Johnson, K. Kendall, A. D. Roberts, *Proc. R. Soc. Lond. Math. Phys. Sci.* **1971**, *324*, 301.
[14] J. Y. He, Z. L. Zhang, H. Kristiansen, *J. Appl. Polym. Sci.* **2009**, *113*, 1398.
[15] Y.-L. Lin, D.-M. Wang, W.-M. Lu, Y.-S. Lin, K.-L. Tung, *Chem. Eng. Sci.* **2008**, *63*, 195.
[16] F. Castro, K. K. Westbrook, J. Hermiller, D. U. Ahn, Y. Ding, H. J. Qi, *J. Eng. Mater. Technol.* **2011**, *133*, 021025.
[17] J. Yin, J. L. Yagüe, D. Eggenspieler, K. K. Gleason, M. C. Boyce, *Adv. Mater.* **2012**, *24*, 5441.
[18] W. M. Choi, J. Song, D.-Y. Khang, H. Jiang, Y. Y. Huang, J. A. Rogers, *Nano Lett.* **2007**, *7*, 1655.
[19] C.-C. Fu, A. Grimes, M. Long, C. G. L. Ferri, B. D. Rich, S. Ghosh, S. Ghosh, L. P. Lee, A. Gopinathan, M. Khine, *Adv. Mater.* **2009**, *21*, 4472.
[20] S.-I. Park, J.-H. Ahn, X. Feng, S. Wang, Y. Huang, J. A. Rogers, *Adv. Funct. Mater.* **2008**, *18*, 2673.
[21] X. Chen, J. W. Hutchinson, *J. Appl. Mech.* **2004**, *71*, 597.
[22] Z. Huang, W. Hong, Z. Suo, *Phys. Rev. E* **2004**, *70*, 030601.
[23] E. Cerda, K. Ravi-Chandar, L. Mahadevan, *Nature* **2002**, *419*, 579.
[24] S. Cai, D. Breid, A. J. Crosby, Z. Suo, J. W. Hutchinson, *J. Mech. Phys. Solids* **2011**, *59*, 1094.
[25] A. V. Tobolsky, J. J. Aklonis, G. Akovali, *J. Chem. Phys.* **1965**, *42*, 723.
[26] B. Wu, A. Heidelberg, J. J. Boland, *Nat. Mater.* **2005**, *4*, 525.
[27] A. S. Argon, R. D. Andrews, J. A. Godrick, W. Whitney, *J. Appl. Phys.* **1968**, *39*, 1899.
[28] D. Vella, A. Ajdari, A. Vaziri, A. Boudaoud, *Phys. Rev. Lett.* **2011**, *107*, 174301.
[29] J. Huang, M. Juszkiewicz, W. H. de Jeu, E. Cerda, T. Emrick, N. Menon, T. P. Russell, *Science* **2007**, *317*, 650.
[30] K. Efimenko, M. Rackaitis, E. Manias, A. Vaziri, L. Mahadevan, J. Genzer, *Nat. Mater.* **2005**, *4*, 293.
[31] M. E. Helgeson, S. C. Chapin, P. S. Doyle, *Curr. Opin. Colloid Interface Sci.* **2011**, *16*, 106.
[32] Z. Yang, W. T. S. Huck, S. M. Clarke, A. R. Tajbakhsh, E. M. Terentjev, *Nat. Mater.* **2005**, *4*, 486.
[33] D. Rodríguez-Fernández, L. M. Liz-Marzán, *Part. Part. Syst. Charact.* **2013**, *30*, 46.
[34] M. Pang, J. Hu, H. C. Zeng, *J. Am. Chem. Soc.* **2010**, *132*, 10771.
[35] C. Xu, B. Wang, S. Sun, *J. Am. Chem. Soc.* **2009**, *131*, 4216.